Experiments in Fluids (2019) 60:172
https://doi.org/10.1007/s00348-019-2811-5

RESEARCH ARTICLE

The magic carpet: an arbitrary spectrum wave maker for internal waves

Thomas E. Dobra[1,2] · **Andrew G. W. Lawrie**[1] · **Stuart B. Dalziel**[2]

Received: 14 June 2019 / Revised: 29 August 2019 / Accepted: 8 September 2019 / Published online: 29 October 2019

Abstract

We present a novel apparatus for generating internal waves of arbitrary size and shape, including both phase-locked and propagating waves. It is an actively driven, flexible "magic carpet" in the base of a tank. Our wave maker is computer-controlled to enable easy configuration. The actuation of a smooth, flexible surface produces clean waveforms with a predictable spectrum, for which we derive a theoretical model. We demonstrate the versatility of our wave maker through an experimental study of linear and nonlinear, isolated, and combined internal waves, including some that are sufficiently nonlinear to break remote from their source.

Graphic abstract

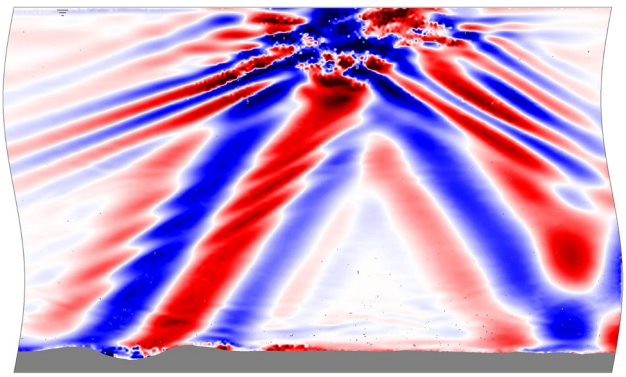

1 Introduction

Internal waves are one of the most important energy transmission systems on Earth: lunar diurnal excitation alone drives around 1 TW of wave power within the world's oceans (Egbert and Ray 2001). This energy causes, for example, the upwelling 2.5×10^7 m^3 s^{-1} of dense, salty water from the deep ocean to the surface, as part of sustaining the meridional overturning circulation (Nikurashin and Ferrari 2013). Internal waves play an essential role in the Earth's climate and laboratory studies provide us with an insight into their properties. In particular, many key natural processes found in internal waves are nonlinear, such as wave breaking (see Staquet and Sommeria 2002), so it is desirable for such experiments to contain internal waves of appreciable amplitude.

The classical way to generate internal waves of a fixed frequency in the laboratory is by oscillating a small object vertically; for example, Görtler (1943), and later Mowbray and Rarity (1967) and Sutherland et al. (1999), used a cylinder with its axis horizontal. In this two-dimensional case, internal waves are emitted equally in the four directions admissible by the dispersion relation. In fact, the

✉ Andrew G. W. Lawrie
andrew.lawrie@bristol.ac.uk

[1] Hele-Shaw Laboratory, University of Bristol, University Walk, Bristol BS8 1TR, UK

[2] Department of Applied Mathematics and Theoretical Physics, University of Cambridge, Wilberforce Road, Cambridge CB3 0WA, UK

object may be oscillated in any direction that displaces fluid vertically; for example, a horizontally oscillating sphere can also emit internal waves (Lin et al. 1994). However, for inviscid, linear internal waves, oscillating an object produces singularities along the characteristics that are tangent to the object, as predicted for cylinders by Hurley (1972, 1997). These singularities introduce a full spectrum including very high wavenumbers and are only regularised by viscosity, which leads to a transition from a bimodal to unimodal profile with distance from the cylinder (Hurley and Keady 1997). Thus, we lose control of the spectrum of the generated internal waves.

A second limitation is that internal wave beams produced by a moving solid body are typically less than one wavelength across, so there is an incomplete picture of any phase-dependent interactions. McEwan (1971, 1973) used an articulated paddle of several straight sections hinged together and mounted on a horizontal shaft to generate two-dimensional standing internal waves with beams several wavelengths in width. However, the paddles are straight sections, which produce a triangular waveform, so again contains a broad spectrum of wavenumbers. Moreover, a new set of paddles would need to be constructed for each desired dominant wavelength.

A significant step forwards towards a controllable, general wave maker was made by Gostiaux et al. (2007). They designed a wave generator actuated by a sequence of cams, each mounted off-centre along a shaft, in a pattern arranged to approximate a travelling sinusoid as the shaft is rotated. For circular cams of the type used in their experiments, the frequency is determined by the shaft rotation rate, the amplitude by the radial offset of the cams, and the wavelength by the phase difference between adjacent cams. The shape they produce has the form:

$$h(x,t) = \sum_n g_n(t)\, H\!\left(\frac{w}{2} - |x - nw|\right), \tag{1}$$

where x is the coordinate along the wave generator, t is time, g_n is the displacement of cam n, w is the spacing between cams, and H is the Heaviside step function. Such a wave generator produces a single beam several wavelengths in width and the amplitude could be set to observe nonlinear effects such as triadic resonance instability (a generalisation of parametric subharmonic instability, Bourget et al. 2013). In addition, Maurer et al. (2017) adapted this apparatus to generate three-dimensional axisymmetric internal waves. However, in both versions, the mechanical linkage makes impossible the alteration of the wave profile during an experiment. Furthermore, the cams produce a staircase approximation (1) to a sinusoid that introduces other wavenumbers to the spectrum, albeit with a cleaner waveform than the paddles of McEwan.

To overcome these limitations, we present the Arbitrary Spectrum Wave Maker (Dobra et al. 2016), which is like a "magic carpet" in the base of the tank, able to produce almost any shape that can be defined as a continuous, single-valued function, $h(x,t)$. Unidirectional sinusoids, solitary humps, and superpositions of multiple frequencies and phase velocities with time-varying amplitudes are all possible.

The apparatus is described in Sect. 2. Complementing the analysis of Mercier et al. (2010) for their cam-driven wave generator, we present a calibrated model in Sect. 3 for the shape obtained by the wave maker surface. In Sect. 4, we discuss the compactness of the Fourier spectrum generated by the wave maker, and we demonstrate the capabilities of the wave maker in Sect. 5.

2 The Arbitrary Spectrum Wave Maker

The Arbitrary Spectrum Wave Maker (ASWaM) is a 1 m-long, flexible section in the base of an 11 m-long tank, and its shape is controlled by an array of low-cost, computer-controlled, linearly actuating stepper motors. We fill the tank with a linear density stratification of the form $\rho_0(z) = \rho_{00} + z\frac{\mathrm{d}\rho_0}{\mathrm{d}z}$, where z is the height above the base of the tank and ρ_{00} is the density at the base of the tank (which in Sect. 4 we will identify as the Boussinesq reference density), using sodium chloride as the solute. The shape of the wave maker is specified in software and can be varied throughout an experiment. By slowly increasing the amplitude of oscillations, large amplitude internal wave perturbations, ρ', can be generated in the liquid without the flow separating near the moving surface. The wave maker is pictured in Figs. 1 and 2 and it is shown schematically, including definitions used in Sect. 3. Early prototypes were surfaced mounted (Lawrie and Dalziel 2014), but although a base-mounted wave maker requires more complex sealing arrangements, it is a more flexible configuration, since the free surface remains unobstructed.

2.1 Mechanical components

The ASWaM consists of a 3 mm-thick nylon-faced neoprene foam sheet (similar to that used for wetsuits) that is deformed by 100 horizontal rods, each spanning the width of the tank. The rods are individually actuated to move vertically and have radius 2 mm and uniform spacing 10 mm. At zero displacement, the wave maker is flush with the base of the tank. Neoprene foam was selected as a matt black, opaque, elastic material that is chemically inert in a salt stratification. Neoprene has some resistance to bending, and this facilitates the creation of smooth, low wavenumber shapes on the wave maker specified by a discrete set of actuation rods.

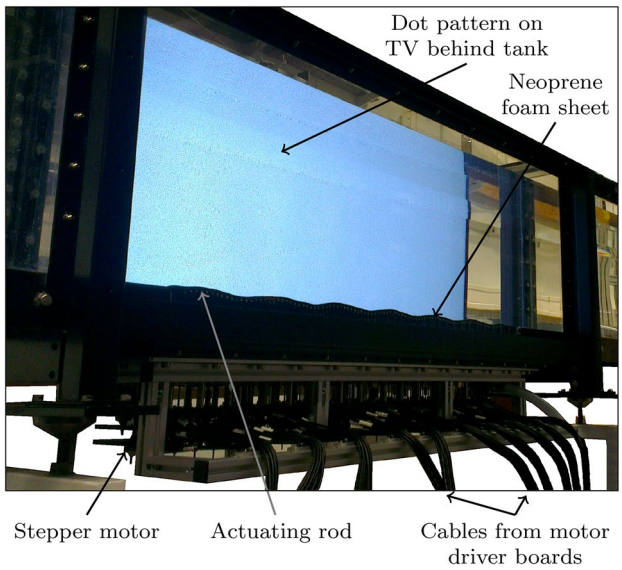

Fig. 1 Arbitrary spectrum wave maker mounted in the base of the tank. The 100 horizontal actuating rods determine the shape of the neoprene foam sheet. They are driven up and down by an array of stepper motors underneath the wave maker. Each motor is powered via its own driver board, which are all out of the field of view. Behind the tank is the dot pattern on the TV screen used for Synthetic Schlieren

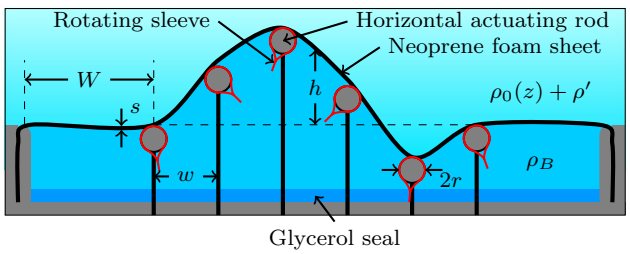

Fig. 2 Longitudinal view of a wave maker shown schematically with six horizontal rods. The cavity underneath the surface of this wave maker is filled with dense, homogeneous salt water of density, ρ_B, with a Boussinesq stratification above the wave maker. A layer of glycerol (dark blue) in the base of the cavity inhibits the ingress of salt down the vertical shafts. The dimensions shown are used in Sect. 3

The lengthwise edges of the sheet are not sealed to the tank wall, so there is an 80 mm-deep cavity of fluid beneath the neoprene and both sides of the sheet are wetted. We thus avoid supporting the full hydrostatic head, so the motors only do work against the dynamic component of the force. Moreover, there is no pressure gradient to drive a leakage flow from the underlying cavity into the working section of the tank, provided the chosen waveform conserves volume. To leading order, three-dimensional effects are limited to wall boundary layers. Beyond the 100 actuators, the two ends of the neoprene foam are clamped at a distance 60 mm from the nearest rod, as sketched in Fig. 2, reducing the severity of gradients between the tank base and the neoprene.

The neoprene is driven by an array of Portescap 26DBM10D1B-L linear stepper motors, each of which has a vertical resolution of 0.0127 mm and a stroke of 48 mm. To minimise heat dissipation from the motors, each is supplied with 0.14 A instead of their rated current of 0.34 A. This reduces the total heat production to 126 W. The lead screw has a tendency to rotate, so a guide rod moves in a sleeve to ensure the actuation is only vertical. The bodies of these motors are too large to be packed in a single line to match the 10 mm pitch of the actuation rods, so to enable a fine horizontal resolution, the motors are staggered in three horizontal and three vertical planes, keeping them as close as possible to the centreline of the wave maker, as shown in Fig. 3.

The neoprene attaches to sleeves around the horizontal rods using hook-and-loop fastener. This facilitates maintenance and can release if the tension in the neoprene foam becomes too great, thereby preventing damage. Furthermore, since the sleeves can rotate about the rods, the contact point of the neoprene varies to minimise the tensile stress in the sheet and the bending moments on the actuators. We find that the wave maker can reliably produce sinusoids of steepness $\left|\frac{\partial h}{\partial x}\right| \leq 0.6$ without the motors stalling or neoprene detaching.

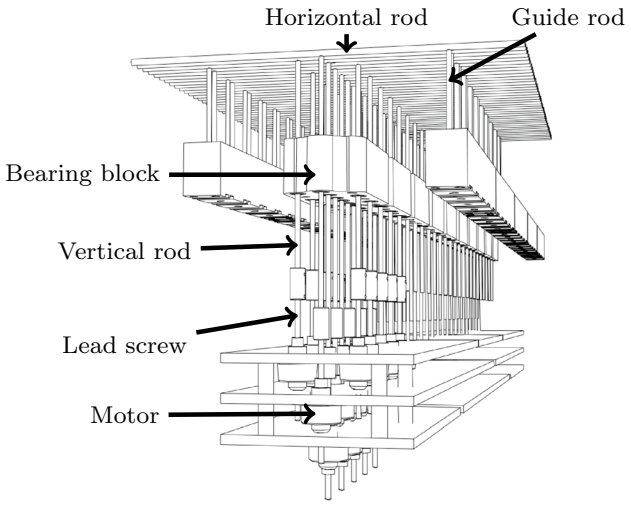

Fig. 3 Perspective drawing of the arrangement of the wave maker linear actuators. The vertical rods are driven up and down, which determines the instantaneous height of each horizontal rod. The neoprene foam sheet of the wave maker is attached to these horizontal rods, so its shape is determined by their heights. The motors are staggered across three horizontal and three vertical planes to enable a tight rod separation of 10 mm

As the motor shafts pass through the base of the cavity, there must be a watertight seal. We use a grease box with a pair of silicone O-rings on either side. Typically, the stratification is created using a salt solution, but inside the cavity, we add glycerol to provide an insulating layer between the salt water and the O-ring seals. The risk with leakage of salt water is that after use, the water evaporates and leaves salt crystals behind, and these can prise open the seals over time. The depth of the glycerol layer is a compromise between prolonging the life of the seals and entraining glycerol into any leakage flow, which might then interfere with optical diagnostic techniques such as Synthetic Schlieren (Dalziel et al. 1998, 2000, 2007; Sutherland et al. 1999). The seals and motor blocks are mounted in modular blocks of ten, to facilitate maintenance.

2.2 Electronics

The low-cost stepper motor driver, which employs a pulsewidth modulation (PWM) to control the current through each of the motor windings, sequences the actuation windings in a half-step mode, which enables us to achieve our fine vertical resolution. For generating the digital input signals, the Texas Instruments Beaglebone Black revision C (BBB) was selected as a low-cost hardware–software interface. It has a Programmable Real-time Unit and Industrial Communication SubSystem (PRU-ICSS) embedded in its Sitara AM3358BZCZ100 processor, on which every instruction takes exactly 5 ns. An efficient assembly-language algorithm uses 15 instructions to issue signals to motor drivers. In the worst case, it might take 1.9 µs to execute all motors simultaneously, but in a typical use-case steps are rarely synchronous and have an effective resolution of 30 ns. This is sufficient temporal resolution to generate smooth waveforms without unwanted additional frequencies in the observable range.

A second key feature of the BBB is its large array of 65 general purpose input/output (GPIO) header pins. Since 200 GPIO pins are required to produce pulse and direction signals for each motor, multiple BBBs are required. To ensure the parallel BBBs remain synchronised with 30 ns precision, thereby avoiding horizontal drift of wave phase between sections of the wave maker, a timing pulse is transmitted along wires from a GPIO pin in one BBB (designated the master) to each of the other (slave) BBBs. This software clock is also written in the assembly language of the PRU-ICSS to minimise latency.

2.3 Software

The software for controlling the wave maker is available at https://bitbucket.org/aswam/wavemaker, with a brief overview here. As discussed in Sect. 2.2, precise timing of the hardware is imperative and accordingly is programmed in assembly. The input instruction set is created using a bespoke compiler that calculates the timings for a waveform specified in text as analytic functions, typically sine waves with some envelope, within an XML file. A web interface using Javascript writes the XML input to the compiler and allows the user to preview their chosen waveform prior to execution on the wave maker. The reader is referred to Dobra (2018, chap. 3) for a detailed discussion of the algorithms.

3 Model of shape of wave maker

We develop an analytic model for the resultant profile of the neoprene carpet for a given input waveform, $h^{\text{in}}(x,t)$. The input only specifies the time-dependent displacement of each rod. The clamps at each end of the wave maker impose a uniform tension along the wave maker, which can be taken as zero when the wave maker is in the equilibrium position.

3.1 Definitions

A schematic of the longitudinal view of the wave maker is shown in Fig. 2. The arbitrary wave maker consists of 100 rods of effective radii r, including the fastening sleeves, with separation w and a gap of W between the last rod and where the elastic sheet is clamped to the tank. The sheet has thickness s, which we assume to be constant. For the ASWaM, $w = 10$ mm, $W = 60$ mm, and $s = 3$ mm, and we find from the calibration of our model (Sect. 3.5) that $r = 4$ mm.

3.2 Governing equations

The neoprene foam sheet is modelled in its linear-elastic regime, under the assumptions of Euler–Bernoulli beam theory, which is valid for waveforms of sufficiently small curvature and when tensile stress is predominantly absorbed by the neoprene rather than the nylon facing. For the maximum wave steepness our wave maker supports, the strain never exceeds 8.5% and the nylon facing only becomes significant at much larger strains and helps prevent damage to the foam by over-extension. Thus, for a neoprene foam sheet clamped at both ends and under tension due to actuation by the rods, we use the elastic theory laid out by Howland (1926) and Kelly (2015). The time-dependent forces and moments per unit width across the tank acting on a short section of the sheet of length $2\,\delta x$ at position x along the wave maker are shown in Fig. 4.

Let θ be the angle the sheet makes with the horizontal and $h(x,t)$ be the vertical displacement of the sheet; then, the trigonometric relation gives θ in terms of h, $\tan\theta = \frac{\partial h}{\partial x}$, and the vertical components of the inviscid hydrodynamic forces become $-2\,\delta x\, p_{\text{A}}(x)\cos\theta \mathbf{e}_z$ and $2\,\delta x\, p_{\text{B}}(x)\cos\theta \mathbf{e}_z$. The static

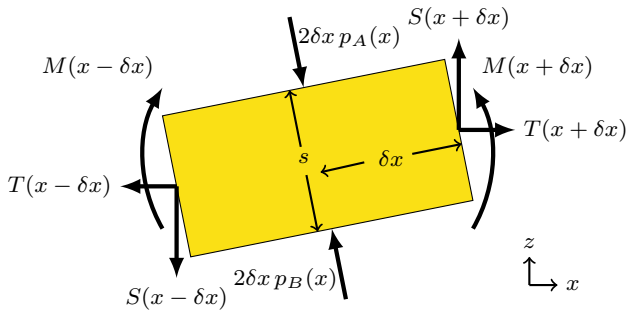

Fig. 4 Forces and moments acting on an element of the sheet (based on Kelly 2015, p. 202). Shear and tension forces are exerted on each end by the neighbouring elements, in addition to a pair of moments. The fluid above and below the sheet exerts a pressure perpendicular to the sheet

equilibrium assumption of Euler–Bernoulli beam theory implies that the horizontal forces, T, vertical forces, S, and moments, M, acting on the element balance:

$$T(x+\delta x) - T(x-\delta x) + 2\,\delta x\, p_{\mathrm{A}}(x)\sin\theta - 2\,\delta x\, p_{\mathrm{B}}(x)\sin\theta = 0, \tag{2a}$$

$$2\delta x\big(p_{\mathrm{B}} - p_{\mathrm{A}}\big)\cos\theta - S(x-\delta x) + S(x+\delta x) = 0, \tag{2b}$$

$$M(x+\delta x) - M(x-\delta x) + \delta x\cos\theta\, S(x+\delta x) + \delta x\cos\theta\, S(x-\delta x) - \delta x\sin\theta\, T(x+\delta x) - \delta x\sin\theta\, T(x-\delta x) = 0. \tag{2c}$$

Let $p_*(x) = p_{\mathrm{B}} - p_{\mathrm{A}}$ be the net pressure, which is zero for static shapes and can be estimated for moving waveforms using linear wave theory. For waves of low steepness $\left(\left|\frac{\partial h}{\partial x}\right| \ll 1\right)$, $\cos\theta \approx 1$, and $\sin\theta \approx \frac{\partial h}{\partial x}$. Then, dividing through by $2\,\delta x$, in the limit $\delta x \to 0$, these become the coupled differential equations:

$$\frac{\partial T}{\partial x} = p_* \sin\theta \approx p_* \frac{\partial h}{\partial x}, \tag{3a}$$

$$\frac{\partial S}{\partial x} = -p_* \cos\theta \approx -p_*, \tag{3b}$$

$$\frac{\partial M}{\partial x} + S - T\frac{\partial h}{\partial x} = 0. \tag{3c}$$

Differentiating the moment Eq. (3c) with respect to x gives

$$\frac{\partial^2 M}{\partial x^2} + \frac{\partial S}{\partial x} - T\frac{\partial^2 h}{\partial x^2} - \frac{\partial T}{\partial x}\frac{\partial h}{\partial x} = 0. \tag{4}$$

Using the horizontal (3a) and vertical (3b) force balances to eliminate the derivatives of the tension and vertical shear forces leaves

$$\frac{\partial^2 M}{\partial x^2} - p_* - T\frac{\partial^2 h}{\partial x^2} + p_*\left(\frac{\partial h}{\partial x}\right)^2 = 0. \tag{5}$$

The fourth term is quadratically smaller than the second, which leaves the linear Euler–Bernoulli beam equation under longitudinal tension:

$$\frac{\partial^2 M}{\partial x^2} - T\frac{\partial^2 h}{\partial x^2} = p_*. \tag{6}$$

In the static case, where $p_* = 0$, our constraint, $\left|\frac{\partial h}{\partial x}\right| \ll 1$, vanishes, implying that our model is valid over the entire operational range of our wave maker. The assumption of linearity is retained in the local curvature, $\left|\frac{\partial^2 h}{\partial x^2}\right|$, respecting both the physical characteristics of the neoprene and Euler–Bernoulli theory.

The tension in each longitudinal fibre of the neoprene is the sum of the externally applied tension, T, which is uniform across the thickness of the sheet, and a perturbation tension, determined by the bending of the sheet. Under this decomposition, the bending moment is the same as for an elastic beam with pure bending, which is proportional to the curvature and Young's modulus, E:

$$M = \frac{Es^3}{12}\frac{\partial^2 h}{\partial x^2}. \tag{7}$$

Assuming that the wave maker remains at sufficiently low steepness for the sleeves around the rods to fully redistribute the longitudinal stress, the external tension is imposed by the clamps at each end of the wave maker plus some local variation due to the dynamic pressure, p_*, given by the horizontal force balance (3a). For a sinusoid, scaling analysis shows that T is an order of magnitude greater than the component of the tension due to the dynamic pressure, so the tension is approximately uniform along the wave maker. Thus, at each instant, the surface, $h(x,t)$, of the wave maker satisfies the forced fourth-order ordinary differential equation (ODE):

$$\frac{Es^3}{12}\frac{\partial^4 h}{\partial x^4} - T\frac{\partial^2 h}{\partial x^2} = p_*. \tag{8}$$

For a complex Fourier mode of amplitude A, wavenumber k and frequency ω that generates an internal wave above the wave maker propagating at an angle Θ to the vertical, p_* is non-zero and the inhomogeneous form becomes

$$\frac{Es^3}{12}\frac{\partial^4 h}{\partial x^4} - \frac{Es|A|^2k^2}{4}\frac{\partial^2 h}{\partial x^2} = p_*, \tag{9}$$

where $p_* = -\frac{A\omega^2}{k}\left(\rho_{\mathrm{B}} + i\rho_{00}\tan\Theta\right)e^{i(kx-\omega t)}$. Real waveforms can be obtained by considering each constituent mode independently and then summing the results.

Defining the bending stiffness coefficient $\alpha = \frac{Es^3}{12}$ and using prime to denote an x derivative, the biharmonic form (8) can be written as

$$\alpha h^{(iv)} - Th'' = p_*, \tag{10}$$

and has general solution

$$h = h_\mathrm{p} + B_0 + B_1 x + B_2 \cosh \lambda x + B_3 \sinh \lambda x, \tag{11}$$

where $\lambda = \sqrt{\frac{T}{\alpha}}$, h_p is the particular integral for p_*, and the coefficients B_j are arbitrary constants to be determined by the boundary conditions. This differs from the typical Euler–Bernoulli solution by the presence of hyperbolic functions instead of cubic polynomials.

3.3 Statement of boundary conditions

The attachment of the neoprene to the actuating rods is complex and worthy of further discussion. There are two forms of flexibility: a vertical elasticity in the hooks and loops, and a rotational freedom of the sleeve around the actuating rod, which helps equilibrate horizontal stresses.

We model the vertical elasticity as a linear spring with tension exerted by the neighbouring sections of the neoprene foam sheet applying vertical force, as shown in Fig. 5. Provided that the local gradient of the prescribed waveform is small, there is negligible lateral forcing on the rod and the vertical forces are given by

$$T_\mathrm{spring} = T \sin\theta_+ + T \sin\theta_-. \tag{12}$$

Approximating the sheet as line segments between a pair of rods j and $j+1$, we obtain

$$\sin\theta \approx \tan\theta = \frac{h^\mathrm{in}_{j+1} - h^\mathrm{in}_j}{w} \approx \frac{\partial h^\mathrm{in}}{\partial x}. \tag{13}$$

We define the spring stiffness to be K and the extension to be $\tilde{r} - r$, where $\tilde{h} = h^\mathrm{in} + (\tilde{r} - r)$, and it follows that

$$\tilde{r} - r \approx \frac{T}{K}\left(\frac{h^\mathrm{in}_{j+1} - 2h^\mathrm{in}_j + h^\mathrm{in}_{j-1}}{w}\right) \approx \frac{Tw}{K}\frac{\partial^2 h^\mathrm{in}}{\partial x^2}. \tag{14}$$

Next, we consider the rotation of the sleeve around the rod. Since the rod spacing is much larger than its radius, $w \gg r$, the radius of curvature of the neoprene is much greater than the effective radius of the rod and so the sheet can be considered straight with an arbitrary constant gradient near the rod. Measured with respect to the rod axis (see Fig. 6), the additional height of the neoprene is given by

$$\tilde{r}_j(\sec\theta - 1) = \tilde{r}_j\left(\sqrt{1 + \tan^2\theta} - 1\right), \tag{15}$$

which we approximate as

$$\tilde{r}_j\left(\sqrt{1 + \left(\frac{\partial \tilde{h}}{\partial x}\right)^2} - 1\right),$$

with a centred finite difference. On the ASWaM, each of these corrections to h above the centre of the rod is not expected to exceed 1 mm, compared to a maximum sinusoidal displacement of 20 mm (or 25.4 mm for other shapes that do not need to be symmetric about $z = 0$).

At each end of the wave maker, there is an extra section of length W that is clamped in a vertical channel, as shown in Fig. 2. At the clamps, the displacement is fixed, $h = 0$.

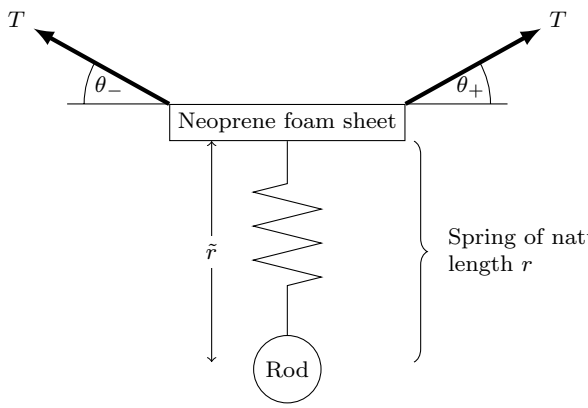

Fig. 5 Model of forces determining the separation between the neoprene foam sheet and a horizontal metal rod. The upper tensions are those applied on this element by neighbouring elements of the sheet. The hook-and-loop fastening that connects the rod to the sheet is modelled as a spring, which is either in tension or compression proportional to its displacement

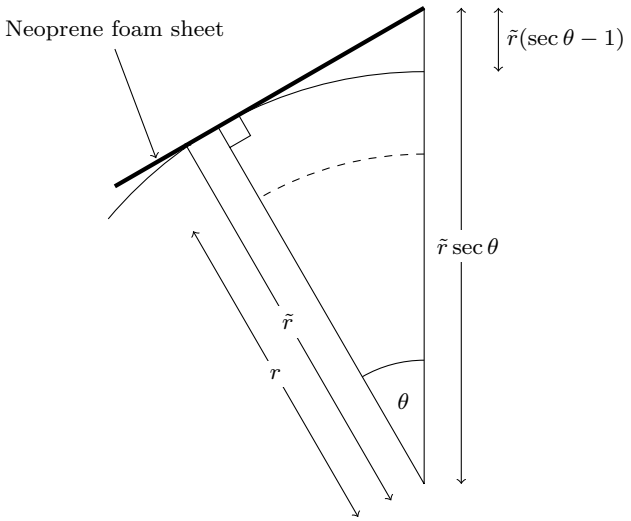

Fig. 6 Variable contact point of the sheet with the rod. For a rod of radius r, the neoprene foam sheet sits at a position given by a larger, variable virtual radius $\tilde{r}$, due to elasticity in the hook-and-loop attachment. Assuming the bending of the sheet is negligible, its height above the centre of the rod increases by $\tilde{r}(\sec\theta - 1)$ as the contact point moves away from the top in either direction

3.4 Basis functions

Each rod imposes a boundary condition on h, thus constraining the values of B_j. The complete system is vastly overdetermined, because there are now 102 such constraints for four constants. We seek to define basis functions that by construction are compatible with all these boundary conditions and to do so we split the wave maker into 101 sections of length d bounded by the rods. Each section should satisfy the biharmonic equation (10) and thus requires four boundary conditions. Two of those are already provided by h being specified at each rod and the remaining two are generated by requiring that h' and h'' are continuous between sections (though their values are not constrained). The end sections are longer, $W = 6w$, so the neoprene foam is approximately straight near the clamps, and to obtain an exactly determined system we constrain $h'' = 0$ (and leave h' unconstrained). Splines would be an inappropriate choice here, because polynomials cannot satisfy the biharmonic equation (10). Instead, we generalise Hermite interpolants to the case of non-polynomial functions to evaluate the shape. The pressure integral, h_p, is computed first, then the constants, B_j, of the complementary functions are calculated to satisfy the four boundary conditions.

Let $\hat{x}$ be the coordinate along each section, with $\hat{x} = 0$ defined on the left end and $\hat{x} = d$ on the right end. For interior sections, $d = w$, and for the two end sections between the final rod and the neoprene clamp, $d = W$. For convenience, rather than directly using the complementary functions:

$$\mathbf{f}(\hat{x}) = \begin{bmatrix} 1 \\ \hat{x} \\ \cosh \lambda\hat{x} \\ \sinh \lambda\hat{x} \end{bmatrix}, \tag{16}$$

we choose four linearly independent linear combinations, expressed as $\mathbf{g} = \mathbf{C}\mathbf{f}$, and select the matrix $\mathbf{C}$ such that g_j and g_j'' are each non-zero at only one end of the segment. In particular, we take

$$\mathbf{G} = \left[\mathbf{g}(0)\ \mathbf{g}''(0)\ \mathbf{g}(d)\ \mathbf{g}''(d)\right] = \mathbf{I}_4, \tag{17}$$

where $\mathbf{I}_4$ is the identity matrix. This choice is motivated by our need to specify h at the junctions between each segment and additionally h'' at the ends of the wave maker. By taking

$$\mathbf{F} = \left[\mathbf{f}(0) \quad \mathbf{f}''(0) \quad \mathbf{f}(d) \quad \mathbf{f}''(d)\right] \tag{18}$$

such that $\mathbf{G} = \mathbf{C}\mathbf{F} = \mathbf{I}_4$, we determine

$$\mathbf{C} = \mathbf{F}^{-1}\begin{bmatrix} 1 & -\frac{1}{d} & 0 & 0 \\ -\frac{1}{\lambda^2} & \frac{1}{\lambda^2 d} & \frac{1}{\lambda^2} & -\frac{1}{\lambda^2 \tanh \lambda d} \\ 0 & \frac{1}{d} & 0 & 0 \\ 0 & -\frac{1}{\lambda^2 d} & 0 & \frac{1}{\lambda^2 \sinh \lambda d} \end{bmatrix}, \tag{19}$$

and then, we obtain the four basis functions:

$$\mathbf{g}(\hat{x}) = \begin{bmatrix} 1 - \frac{\hat{x}}{d} \\ -\frac{1}{\lambda^2} + \frac{\hat{x}}{\lambda^2 d} + \frac{\cosh \lambda\hat{x}}{\lambda^2} - \frac{\sinh \lambda\hat{x}}{\lambda^2 \tanh \lambda d} \\ \frac{\hat{x}}{d} \\ -\frac{\hat{x}}{\lambda^2 d} + \frac{\sinh \lambda\hat{x}}{\lambda^2 \sinh \lambda d} \end{bmatrix}. \tag{20}$$

Defining a vector of constants $\mathbf{b}$ to be determined by the boundary conditions, the general solution between each rod is thus

$$h(\hat{x}) = h_p(\hat{x}) + \mathbf{b} \cdot \mathbf{g}(\hat{x}). \tag{21}$$

In common with cubic Hermite interpolation polynomials (cubic splines), our interpolation functions form pairs that are reflections of themselves. The functions g_0 and g_2 are straight lines, providing the continuity of the sheet, while g_1 and g_3 (see Fig. 7) give the curvature arising from the bending stiffness, thereby enabling C^2 continuity.

In the regime of low bending stiffness, $\alpha \to 0$ and $\lambda \to \infty$, the turning points of g_1 and g_3 move nearer the end points of the section and their magnitudes decrease; in other words, they become closer to constant zero functions. This degenerate behaviour arises from the bending term, $\alpha h^{(iv)}$, in the biharmonic equation (10) vanishing, hence the reduction of the equation from fourth order to second order.

In the opposite limit of large bending stiffness, $\lambda \to 0$, Eq. (10) is again degenerate, as the term Th'' vanishes. Using Taylor expansions, it can be shown that the bending basis functions reduce to cubic polynomials:

$$g_1 \sim -\frac{\hat{x}^3}{6d} + \frac{\hat{x}^2}{2} - \frac{\hat{x}d}{3}, \qquad g_3 \sim \frac{\hat{x}^3}{6d} - \frac{\hat{x}d}{6}. \tag{22}$$

These are generalised first-order (cubic) Hermite interpolation polynomials when the zeroth and second derivatives are specified.

The boundary conditions across all sections of the wave maker form a linear system of 404 simultaneous equations for all of the 101 constant vectors, $\mathbf{b}$. The system is sparse

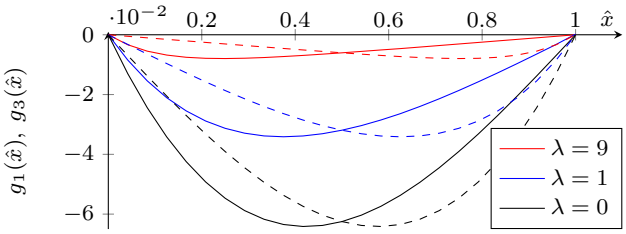

Fig. 7 Curvature basis functions for the surface of the wave maker shown at various shape parameters, λ using a unit rod spacing ($d = 1$). The solid lines show the basis function g_1 and the dashed lines show its reflection, g_3. The curves become cubic in the large bending stiffness case when $\lambda = 0$

and can be reduced to a simpler system of 101 coupled equations using the symmetries of the basis functions, and be solved numerically. In the case of a static Fourier mode (for which $p_* = 0$), an analytic solution can be obtained using recurrence relations. We refer the reader to Dobra (2018, Chap. 3) for details.

3.5 Calibration and verification of model

We tested the model experimentally on four classes of static waveform by illuminating the centreline of the wave maker using a FLEXPOINT® MVnano laser diode of wavelength 520 nm and fan angle 30°. We filmed the laser profile through the side wall of the tank using an ISVI IC-X12CXP 12-megapixel camera (Fig. 8 shows a typical image), making appropriate ray-path corrections for refractive index variations, as illustrated in Fig. 9. The tank was completely filled with fresh water to minimise distortion of the image. Under these conditions, internal waves cannot be generated, so the parts of the model that introduce pressure corrections due to internal waves have not been included in this test; here, we restrict to cases with $p_* = 0$, which correspond to static waveforms.

Five types of waveform were tested: a single rod raised with all other rods at the zero position (Fig. 8), a single rod lowered, all the rods on one half of the wave maker raised by a uniform amount (Heaviside step), and two sinusoids, one of wavenumber 100 rad m^{-1} and the other of wavenumber 20 rad m^{-1}. The amplitudes were increased by 1.27×10^{-3} m (100 motor steps) between each consecutive image until the reliable limit of the wave maker had been obtained, typically due to the motors stalling when unable to further increase the tension in the neoprene foam. This ensures that the full range of typical configurations are tested. A sample output is shown in Fig. 10.

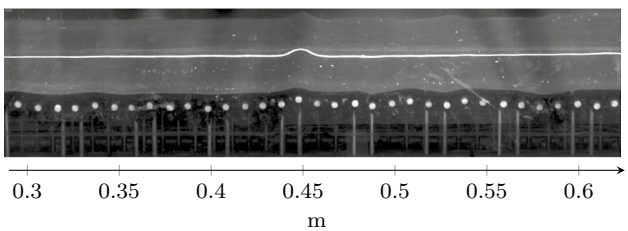

Fig. 8 Raw image of the laser (white line) on the centreline of the wave maker with one rod raised by 5.08 mm. Illuminating the centreline records the average height across the wave maker and accounts for small variations in transverse slope along each horizontal rod. The compactness of the stitching of the hook-and-loop fasteners varies from rod to rod and is calibrated out to ensure a smooth fluid-facing surface. The rods themselves, therefore, vary in height to produce this, as can be seen in the figure

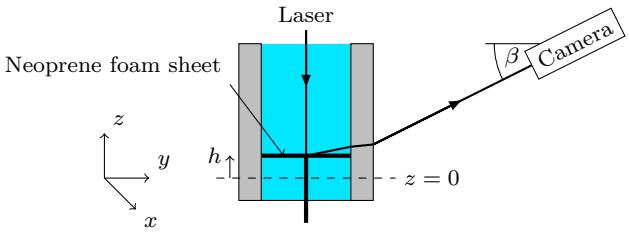

Fig. 9 Apparatus for optically measuring height of wave maker. A line laser illuminates the centreline of the wave maker from above, which is recorded through the transparent side wall of the tank by a camera

We were surprised to discover that neoprene foam—a mildly anisotropic material—has an unusual relationship between bending stiffness, governed by α, and tensile stresses, governed by T, and a consequence of this is that the ratio $\lambda = \sqrt{\frac{T}{\alpha}}$ is approximately constant. We find that λ is logarithmically insensitive to changes in the solution, and we obtain $\lambda = 400 \pm 25$. It follows that $T \propto Es^3$ and the thickness, s, can be reasonably assumed not to increase with T. We hypothesise that cells forming the foam collapse progressively under tension and can, therefore, resist Poisson's ratio contraction more effectively, yielding an apparent increase in the Young's modulus with respect to bending. Furthermore, we note that the coupled parameter $(T/K) = (9 \pm 1) \times 10^{-4}$ m is also a constant (thus, as tension increases, the hook-and-loop fasteners become stiffer) and the equilibrium effective rod radius is $r = 4 \times 10^{-3}$ m. Conveniently, the invariance of these parameters directly implies invariance of the wave maker response to any input waveform.

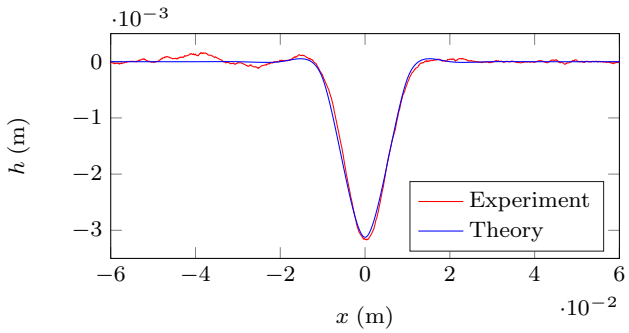

Fig. 10 Comparison of theory with profile recorded on the apparatus for one rod of the wave maker displaced down by 3.81×10^{-3} m. The prediction has a small RMS error of 4×10^{-5} m and exhibits the small humps around $x = \pm 1.3 \times 10^{-2}$ m, which result from the bending stiffness

4 Finite approximations to infinite plane waves

We aim to be able to produce waveforms that are as close to monochromatic as possible within the confines of the laboratory. Only a plane wave with periodic boundaries or boundaries at infinity can truly satisfy this condition. Any wave with a fundamental wavenumber k_0, but of finite spatial width, will contain a full spectrum of wavenumbers even if it has a single temporal frequency, because any deviation away from uniformly zero amplitude involves a local discontinuity in at least one of the derivatives.

In Fourier space, the integral operator is $1/ik$, where i is the imaginary number. Given that the Fourier transform of a Dirac δ-function is a constant, by integrating $\delta(x)$ twice, we obtain a C^0 continuous function, whose spectral signal must decay as $|k|^{-2}$. By induction, the general case follows a power law $C^q \mapsto |k|^{-(q+2)}$. Typically, such waveforms have a symmetric spectrum around k_0, and therefore, this will include both positive and negative wavenumber components. The negative components produce a wave travelling in the opposite direction to k_0.

For the piecewise constant cam-driven wave generator of Gostiaux et al. (2007), their C^{-1} continuity means that the spectrum only decays as $|k|^{-1}$. In contrast, the C^2 continuity imposed by our neoprene foam leads to a decay as $|k|^{-4}$, reducing the spectral spread and producing a cleaner waveform. However, further refinements can be made by profiling the amplitude envelope towards each end of the wave maker, maximising the smoothness of the output waveform, an approach previously pursued by Mercier et al. (2010). We have used a range of candidate input functions in our experiments: trapezia with piecewise linear $\left(C^0\right)$ and half cosine $\left(C^1\right)$ ends and a smoother C^1 envelope comprised of a single wavelength of $\cos^2 x$. For the range of k_0 used in our experiments, the piecewise linear ramp has lower amplitude in wavenumbers immediately surrounding k_0 compared with the half cosine; however, it has higher amplitudes for small negative k. Nonetheless, with all wave maker outputs C^2 continuous by design, improving the input continuity to C^3 has little observable effect on the output spectrum and these details are not significant for most applications. The $\cos^2 x$ input envelope has a noticeably more compact spectrum than the trapezia, but has lower response at k_0 and has no region of constant amplitude. For comparison, in Fig. 11, we show instantaneous profiles, their envelopes and spectra for the following cases: a piecewise linear trapezium input, its corresponding model output (which differs only in the extremities) and the output for a $\cos^2 x$ envelope.

Care must be taken to ensure overall volume conservation in the chamber underneath the neoprene, and we find this is typically satisfied to ± 40 ml when the profile contains an integer number of wavelengths and the length of the ramp is calibrated accordingly. Inevitably, the finite spacing of actuators also broadens the spectrum, but this is mitigated first by selecting low values of k_0 and second by the C^2 continuity of the material. The smoothness of the deforming material surface is a key feature of our wave maker. When waves grow to large amplitude, inertial effects do become significant near the surface and without sufficient smoothness, flow separation may result. As later results in Sect. 5 show, we can produce very large amplitudes with our design with relatively little flow separation occurring.

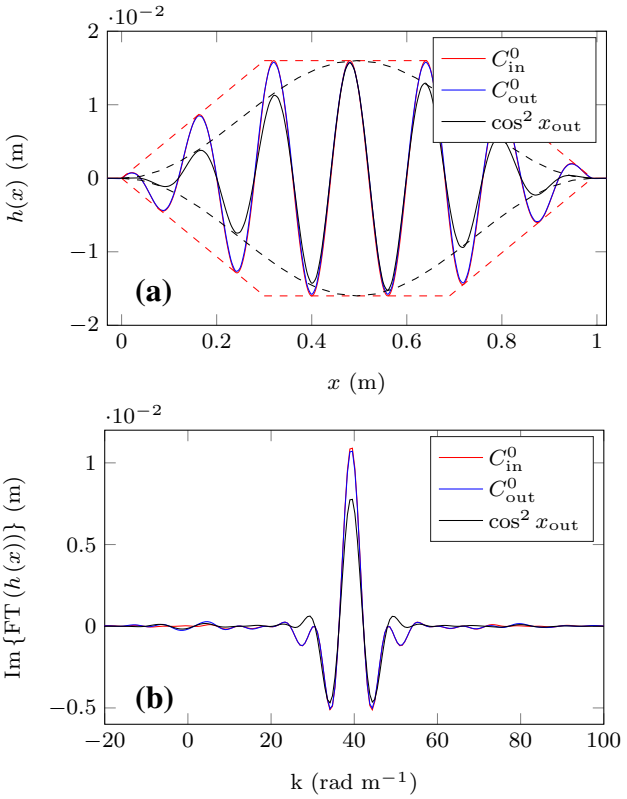

Fig. 11 Instantaneous shapes and spectra for two classes of amplitude envelope for a travelling sinusoid with $k_0 = \frac{2\pi}{\frac{1}{6}\times 0.96} \approx 39.3\,\text{rad}\,\text{m}^{-1}$. The red line shows the input that produces the blue output waveform; there is very little difference (RMS error $= 4.7 \times 10^{-4}$ m), except for a slight reduction in amplitude due to the elasticity in the rod attachments

Although our wave maker attempts to produce waves of the form $A \sin\left(k_0 x - \omega t\right)$, the existence of negative wavenumbers in the spectrum means that waves will also travel backwards. The narrower the region of non-zero amplitude, the broader the spectrum and the more energy will travel in the negative direction. The breadth of the spectrum has particular significance

when generating internal waves, which propagate away from the wave maker into the density-stratified medium, because the manner in which different Fourier components interact nonlinearly is still not fully understood and this has been one motivation for our study. We will introduce the underlying mechanisms of these nonlinear processes in Sect. 5.2.

Two-dimensional linear internal waves are a restricted solution of the Navier–Stokes equations in the case, where we assume inviscid, Boussinesq flow (with reference density ρ_{00}) and the nonlinear terms, which contain the advection operator $\mathbf{u}\cdot\nabla$, are considered negligible. The remaining derivative operators can be isolated into a complex matrix $\mathbf{P}$ that acts on a state vector $\boldsymbol{\phi}$, say, and the system arranged into homogeneous form. Taking a single Fourier mode of $\boldsymbol{\phi}$, we can write

$$\boldsymbol{\phi} = \hat{\boldsymbol{\phi}}\, e^{i(\mathbf{k}\cdot\mathbf{x}-\omega t)}, \tag{23}$$

where $\mathbf{k} = \begin{bmatrix} k & m \end{bmatrix}^T$ and $\mathbf{x} = \begin{bmatrix} x & z \end{bmatrix}^T$. The derivative operator $\mathbf{P}$ then takes the complex algebraic form $\hat{\mathbf{P}}$. For a homogeneous system, non-trivial symmetries are found when the determinant $\left|\hat{\mathbf{P}}\right| = 0$, and these correspond to resonant wave behaviours. From

$$\left|\hat{\mathbf{P}}\right| = \omega^2 - \left(-\frac{g}{\rho_{00}}\frac{d\rho_0}{dz}\right)\frac{k^2}{|\mathbf{k}|^2} = 0 \tag{24}$$

arises a natural frequency, the buoyancy (Brunt–Väisälä) frequency:

$$N = \sqrt{-\frac{g}{\rho_{00}}\frac{\mathrm{d}\rho_0}{\mathrm{d}z}}, \tag{25}$$

and by examining the geometry of $\frac{k}{|\mathbf{k}|}$, a dispersion relation:

$$\omega = N\cos\Theta, \tag{26}$$

is obtained, where Θ is the angle between wavevector $\mathbf{k}$ and the horizontal. Further examination of the properties of (24) shows that waves travel through a density-stratified medium in beams perpendicular to $\mathbf{k}$.

Although the inviscid theory represents the leading-order behaviour of internal waves, our experiments, which we will present in Sect. 5, do show some viscous attenuation. For example, the low-frequency beam spanning the width of Fig. 15 is seen to have its amplitude decreased to a third of its original value over a distance of 1 m. This is consistent with estimates in the literature (Hurley and Keady 1997; Sutherland 2010), where the amplitude A decays with beam ordinate ζ as

$$A(\zeta) = A(0)e^{-\frac{\nu|\mathbf{k}|^3}{2N\sin\Theta}\zeta}, \tag{27}$$

where ν is the kinematic viscosity. On the scale of our experiments, this is acceptably small to ignore as a second-order effect.

When actuating the wave maker, we have an arbitrary choice of k and ω, so we may represent an arbitrary spectrum of travelling wave material surface displacements. Typically, however, we oscillate the wave maker at a common (temporal) frequency for all (spatial) wavenumbers. The surface spectrum specifies the horizontal components of 2D wavevectors for any internal waves produced, and the vertical component thereof is determined to satisfy the angle Θ of that wavevector, as constrained by the choice of ω in the dispersion relation (26). For a broad surface spectrum that includes negative wavenumbers, internal waves leaving the wave maker must travel in two distinct directions: one beam in each upper quadrant (Baines 1971). In practice, nonlinearity gives rise to additional harmonics generated by the boundary, a topic explored by Dobra (2018) that we intend to publish at a later date.

An example of the complexity that can arise from forcing by the wave maker is shown in Fig. 12, using Synthetic Schlieren to infer motion from optical measurements of density perturbations. By selecting a spatially compact forcing (here a single wavelength) and a low forcing frequency, $\omega = 0.108$ N, the dispersion relation permits nine harmonics, all of which are visible, along with significant energy travelling in the $-k_0$ direction. By contrast, a carefully configured wave maker input produces an almost-monochromatic wave, shown in Fig. 13, with almost no energy propagating in the $-k_0$ direction and only a very weak signal in the second harmonic propagating up and to the right. All experimental observations show a subsection of the tank near the wave maker, and are displayed with unit aspect ratio and a length scale measured from the left end of the wave maker.

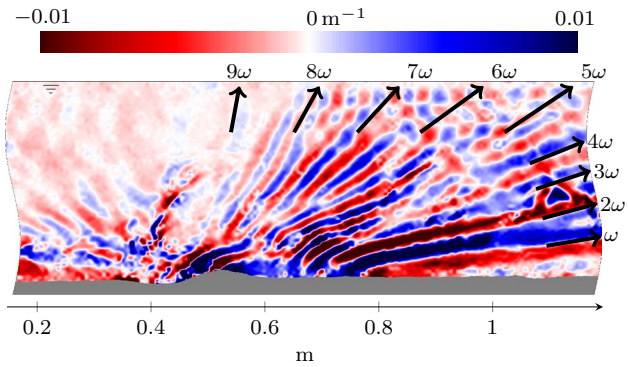

Fig. 12 Horizontal gradient of the normalised density perturbation $\frac{1}{\rho_{00}}\frac{\partial\rho'}{\partial x}$ for a sinusoid of amplitude 0.018 m with a $\cos^2 x$ envelope, $k_0 = 20\,\mathrm{rad\,m^{-1}}$ and $\omega = 0.19\,\mathrm{rad\,s^{-1}} \approx 0.108$ N. The narrow active zone produces a broad spectrum of waves with both positive and negative wavenumbers, including nine harmonics

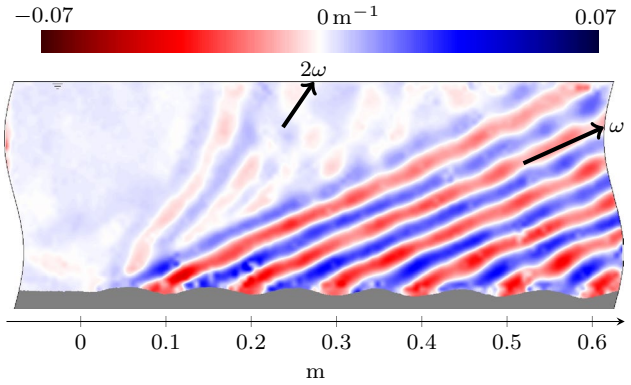

Fig. 13 Clean horizontal gradient field of the normalised density perturbation $\frac{1}{\rho_{00}}\frac{\partial \rho'}{\partial x}$ for a sinusoid of amplitude 0.005 m with $k_0 = 60\,\mathrm{rad\,m^{-1}}$ and $\omega = 0.6\,\mathrm{rad\,s^{-1}} \approx 0.41\,\mathrm{N}$

5 Example wave fields

In this section, we present a sample of results showcasing the flexibility of our experimental tool. None of the configurations shown would have been possible with devices reported in the previous literature. We first discuss our analogue of atmospheric lee waves before considering weakly nonlinear interactions of internal wave beams. By increasing amplitude, we begin to access a strongly nonlinear regime in which wave-breaking events may occur.

5.1 Lee waves

When density-stratified flow is displaced vertically over a mountain, internal lee waves form (Scorer 1949). A phase-locked wave train is created behind the obstacle, in accordance with the measurements of Dalziel et al. (2011). They used a closed-loop flume containing an obstacle to examine lee wave formation in the low Froude number regime. However, those results were contaminated by boundary layer growth and startup transients. Our configuration holds the medium quiescent, and we generate lee waves by propagating a solitary hump along our wave maker, as shown in Fig. 14. Unaffected by boundary layer growth, we have very precise control over the spectral signature. In our case, transients do occur due to the creation of the hump at one end of the wave maker, but near-steady-state lee waves are observed towards the opposite end. Many other shapes and velocity profiles could, of course, also be specified to represent more general topographic features.

5.2 Interacting beams

Weakly nonlinear interactions of internal waves arise from the quadratic nonlinearity in the transport terms of the Navier–Stokes equations (Phillips 1960; Martin et al. 1969; Tabaei et al. 2005). They are best understood in Fourier space, where the velocity term can be expressed in the following form:

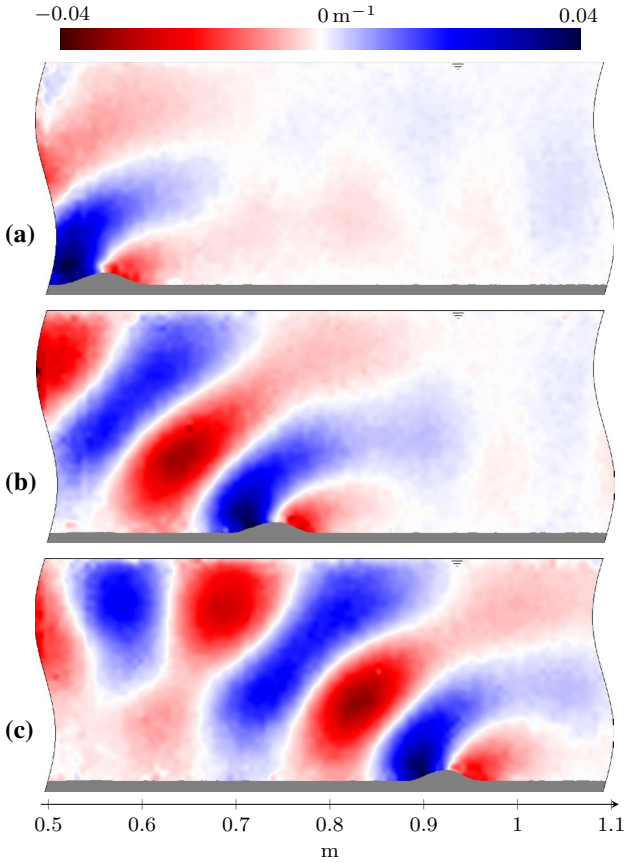

Fig. 14 Horizontal gradient of the normalised density perturbation $\frac{1}{\rho_{00}}\frac{\partial \rho'}{\partial x}$ for a solitary sinusoidal hump of height 0.0075 m and width 0.09 m moving at 0.17 m s^{-1}. Each image is separated by 5 s, and $N = 1.45\,\mathrm{rad\,s^{-1}}$

$$\mathbf{u} = \sum_p \hat{\mathbf{u}}_p e^{i(\mathbf{k}_p \cdot \mathbf{x} - \omega_p t)}. \tag{28}$$

Its gradient

$$\nabla \mathbf{u} = \sum_q i \hat{\mathbf{u}}_q \mathbf{k}_q e^{i(\mathbf{k}_q \cdot \mathbf{x} - \omega_q t)}, \tag{29}$$

combines as follows:

$$\mathbf{u} \cdot \nabla \mathbf{u} = \sum_p \sum_q i \hat{\mathbf{u}}_q \left(\mathbf{k}_q \cdot \hat{\mathbf{u}}_p\right) e^{i((\mathbf{k}_p + \mathbf{k}_q)\cdot \mathbf{x} - (\omega_p + \omega_q)t)}, \tag{30}$$

where we recognise the sums of wavevectors and corresponding frequencies to be new, independent wave directions. We also have to consider the complex conjugates and so there exist pairings of wavevectors and frequencies whose combination satisfy the dispersion relation (26), including those arising from

$$\mathbf{k}_r = \mathbf{k}_q - \mathbf{k}_p \tag{31a}$$

$$\omega_r = \omega_q - \omega_p. \tag{31b}$$

Should the collision of two accordingly configured internal waves p' and q' occur, we would expect emission of this particular wave r'.

For example, the configuration shown in Fig. 15 has incident frequencies $\omega_{p'} = 0.55\,\mathrm{rad\,s^{-1}} \approx 0.37\,\mathrm{N}$ and $\omega_{q'} = 2.2\omega_{p'} \approx 0.82\,\mathrm{N}$ with corresponding dominant horizontal wavenumbers $k_{p'} = 55\,\mathrm{rad\,m^{-1}}$ and $k_{q'} = 2.2k_{p'} = 121\,\mathrm{rad\,m^{-1}}$. We reflect the lower frequency wave, p', off the free surface so that it approaches from the opposite vertical direction. We see from the figure that a new internal wave r' is clearly generated in the interaction region, having not propagated in from the boundaries. It has frequency $\omega_{r'} = \omega_{q'} - \omega_{p'} = (2.2-1)\omega_{p'}$ and the beam is directed exclusively into the first quadrant, in agreement with the correction of Jiang and Marcus (2009) to the theory of Tabaei et al. (2005), and the experiments in Smith and Crockett (2014).

On detailed examination, we note that an oscillation of frequency $\omega_{q'} - \omega_{p'}$ and wavevector $\mathbf{k}_{q'} - \mathbf{k}_{p'}$ does not satisfy the dispersion relation (26), so cannot propagate as an internal wave. However, a new internal wave is, nevertheless, produced, but $\mathbf{k}_{r'} \neq \mathbf{k}_{q'} - \mathbf{k}_{p'}$. This demonstrates that wavevectors across the spectrum of a spatially narrow beam participate in the interaction, not just the dominant $\mathbf{k}_{p'}$ and $\mathbf{k}_{q'}$, which makes it especially important to have a good quantification of the input spectrum. Also visible in the figure is the second harmonic of the leftmost-generated wave, which reflects off the free surface and interacts with its fundamental.

5.3 Wave breaking

We sought to explore amplitude extremes with our wave maker while preserving attached flow for as long as possible. High amplitude internal waves cease to conform to linear theory, and this is an area ripe for further investigation. We began with a standing sinusoid of horizontal wavenumber $k_0 = 33\,\mathrm{rad\,m^{-1}}$ and frequency $\omega = 0.63\,\mathrm{rad\,s^{-1}} \approx 0.5\,\mathrm{N}$, initialised from rest and grown linearly to reach steady oscillations at an amplitude of $A = 0.015$ m, as shown in Fig. 16. The configuration had a wave steepness of $\left|\frac{\partial h}{\partial x}\right|_{\max} = Ak_0 = 0.5$, just below the wave maker limit identified in Sect. 2.1. Initially (Fig. 16a, $A = 0.0076$ m), an interference pattern of left- and right-travelling waves was created in the centre of the tank. With increasing amplitude, there was progressive loss of coherence in the pattern as nonlinearity became visible around $A = 0.0126$ m (Fig. 16b). At full amplitude (Fig. 16c), the Synthetic Schlieren diagnostic showed incoherent patches. These were caused by large curvature in the density field, and hence the refractive index. They make the light rays incident on the camera cross one another, breaking the assumption of a bijection between visible points on the background image and its projection. Direct observation showed that the large curvature was caused by local patches of turbulent mixing. These patches originate where waves have broken (leading to material surfaces that are multivalued in the vertical and so are Rayleigh–Taylor unstable) and these modify the background stratification, tending to generate intrusions that propagate horizontally as they return to hydrostatic equilibrium.

Standing waves are not the only approach to wave breaking with our wave maker: we input a spatially narrow incident beam, expecting that the breadth of its spectrum

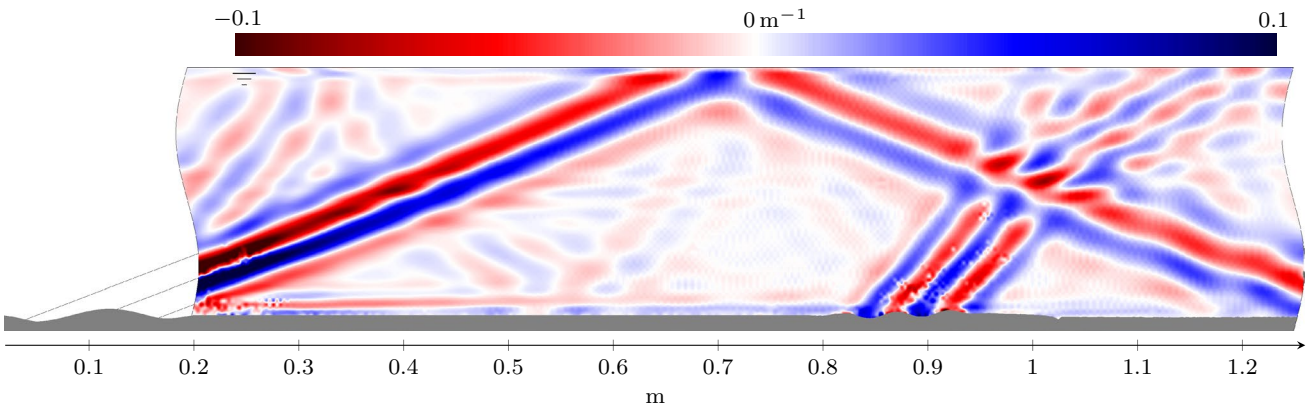

Fig. 15 Vertical gradient of the normalised density perturbation $\frac{1}{\rho_{00}}\frac{\partial \rho'}{\partial z}$ for two incident wave beams, $\omega_{p'} = 0.55\,\mathrm{rad\,s^{-1}} \approx 0.37\,\mathrm{N}$ generated on the left and $\omega_{q'} = 2.2\omega_p$ generated on the right end of the wave maker, crossing in the right half of the field of view. A new wave $\omega_{q'} - \omega_{p'}$ is emitted, in addition to other triadic interactions elsewhere

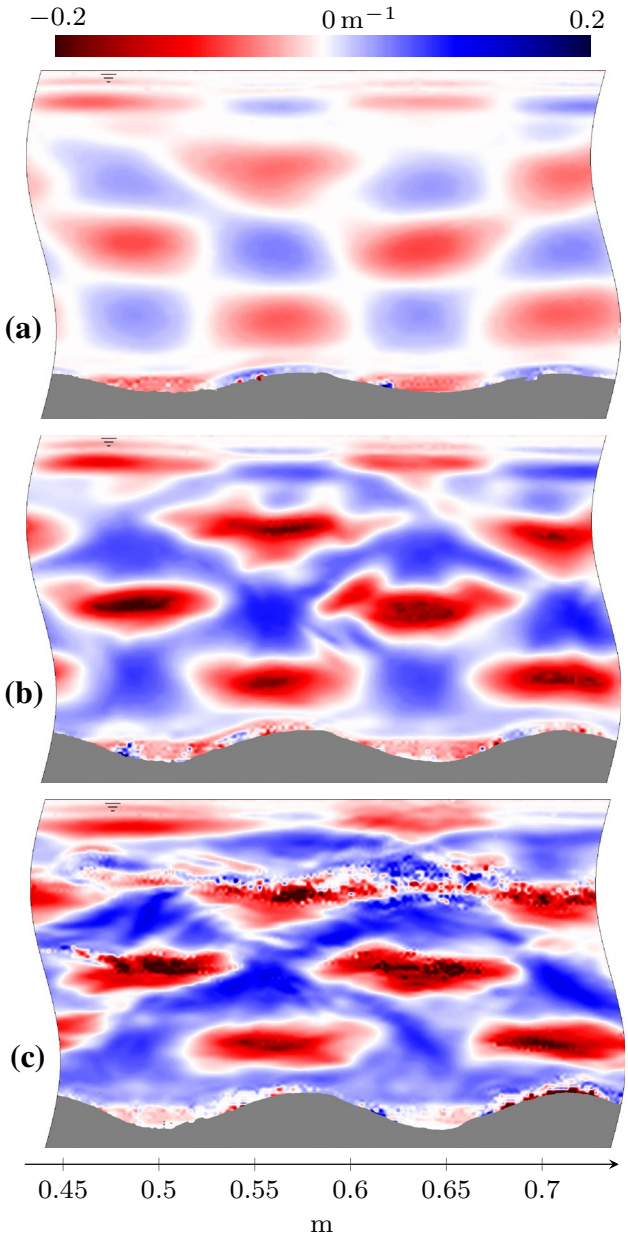

Fig. 16 Vertical gradient of the normalised density perturbation $\frac{1}{\rho_{00}}\frac{\partial \rho'}{\partial z}$ for a standing sine wave of linearly growing amplitude until 0.015 m is attained. The instantaneous amplitudes are 0.0076 m (**a**), 0.0126 m (**b**), and 0.015 m (**b**), with a time interval of 100 s between images. The standing wave pattern progressively modulates and then breaks. In **c**, small hydraulic jumps are responsible for small changes to the background stratification in immediate proximity to the wave maker; these are only significant at very high wave amplitudes

would produce even richer phenomena. Figure 17 shows a wave field that breaks on reflection from the free surface. The sinusoid is two wavelengths wide, with frequency $\omega \approx 0.84$ N, horizontal wavenumber $k_0 = 50$ rad m^{-1} and a $\cos^2 x$ amplitude envelope. Similar to our other experiments, we slowly increased the amplitude from rest at a constant

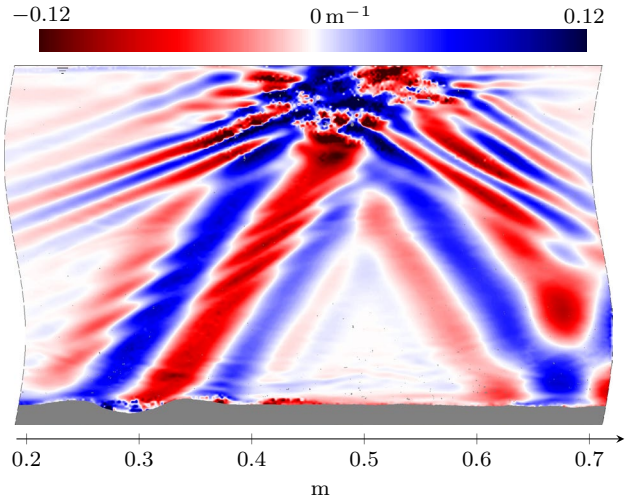

Fig. 17 Vertical gradient of the normalised density perturbation $\frac{1}{\rho_{00}}\frac{\partial \rho'}{\partial z}$ showing the breaking of an internal wave (top-centre) of angular frequency $\omega = 1.5$ rad s^{-1} ≈ 0.84 N, incident from the bottom-left. New internal waves are emitted from the breaking zone at lower frequencies, both to the left and to the right

rate of 0.001 m min^{-1}, which equates to 7×10^{-5} m per period, helping to inhibit the formation of a turbulent boundary layer on the wave maker surface. At the instant shown in Fig. 17, the forcing amplitude was 0.0088 m.

An important feature of the wave-breaking event shown here is the emission of new internal waves at frequencies below the incident frequency. In fact, the lowest of those is the limiting case of zero frequency and arises due to unstable overturning of isopycnals that produces irreversible mixing and material transport. In other contexts, these displacements may be known as intrusive gravity currents, and their signature can be identified in the figure near the free surface. Any displacement of mass, whether oscillatory or aperiodic, distorts material surfaces in equivalent ways to imposed boundary conditions such as our wave maker. In the case shown, material surfaces bounding the wave-breaking region configure to generate a multiplicity of new internal waves. It can be shown that waves are emitted in all four quadrants in a manner analogous to the classical oscillating cylinder of Mowbray and Rarity (1967). However, the frequencies of those waves turn out to be inconsistent with straightforward triadic interactions of the form (31), and therefore, they must emerge from a more complex nonlinear process, as a patch of turbulence would provide. Also visible in this figure is a weakly nonlinear instability of the primary beam due to the well-known phenomenon of triadic resonant instability (Davis and Acrivos 1967), and the example here is typically classified as parametric subharmonic instability. This is separated in space,

independent from and at a much lower amplitude than the strongly nonlinear features closer to the free surface.

6 Conclusion

We have presented a novel wave maker capable of generating large amplitude internal waves of arbitrary shape, configured purely through a software interface. Our wave maker produces clean, reproducible spectra, which we have modelled and validated. We have demonstrated our new capability to produce various forms of time-varying material surface deformation, and we use this to increase the wave amplitude without inducing significant flow separation, such that these waves may break remote from their source or interact nonlinearly. There is a rich collection of fluid phenomena yet to be discovered that we will now be able to access using this new technology.

References

Baines PG (1971) The reflexion of internal/inertial waves from bumpy surfaces. J Fluid Mech 46(2):273–291

Bourget B, Dauxois T, Joubaud S, Odier P (2013) Experimental study of parametric subharmonic instability for internal plane waves. J Fluid Mech 723:1–20

Dalziel SB, Hughes GO, Sutherland BR (1998) Synthetic schlieren. In: Proc. 8th Int. Symp. Flow Vis

Dalziel SB, Hughes GO, Sutherland BR (2000) Whole-field density measurements by 'synthetic schlieren'. Exp Fluids 28(4):322–335

Dalziel SB, Carr M, Sveen JK, Davies PA (2007) Simultaneous synthetic schlieren and PIV measurements for internal solitary waves. Meas Sci Technol 18(3):533–547

Dalziel SB, Patterson MD, Caulfield CP, Le Brun S (2011) The structure of low-Froude-number lee waves over an isolated obstacle. J Fluid Mech 689:3–31

Davis RE, Acrivos A (1967) The stability of oscillatory internal waves. J Fluid Mech 30(4):723–736

Dobra TE (2018) Nonlinear Interactions of Internal Gravity Waves. PhD thesis, University of Bristol

Dobra TE, Lawrie AGW, Dalziel SB (2016) Nonlinear interactions of two incident internal waves. In: Proc. VIIIth Int. Symp. Stratif. Flows, San Diego, USA

Egbert GD, Ray RD (2001) Estimates of M_2 tidal energy dissipation from TOPEX/Poseidon altimeter data. J Geophys Res Ocean 106(C10):22475–22502

Görtler H (1943) Über eine Schwingungserscheinung in Flüssigkeiten mit stabiler Dichteschichtung. ZAMM Zeitschrift für Angew Math Mech 23(2):65–71

Gostiaux L, Didelle H, Mercier S, Dauxois T (2007) A novel internal waves generator. Exp Fluids 42(1):123–130

Howland RCJ (1926) LVII. The vibrations of rods and shafts with tension or end-thrust. London Edinburgh Dublin Philos Mag J Sci 1(3):674–694

Hurley DG (1972) A general method for solving steady-state internal gravity wave problems. J Fluid Mech 56(4):721–740

Hurley DG (1997) The generation of internal waves by vibrating elliptic cylinders. Part 1. Inviscid solution. J Fluid Mech 351:105–118

Hurley DG, Keady G (1997) The generation of internal waves by vibrating elliptic cylinders. Part 2. Approximate viscous solution. J Fluid Mech 351:119–138

Jiang CH, Marcus PS (2009) Selection rules for the nonlinear interaction of internal gravity waves. Phys Rev Lett 102:124502

Kelly P (2015) An introduction to solid mechanics. University of Auckland

Lawrie AGW, Dalziel SB (2014) Analysis of internal wave systems of complex form generated from a flexible boundary. In: Conf. Nonlinear Eff. Intern. Waves, Cornell University, Ithaca

Lin Q, Boyer DL, Fernando HJ (1994) Flows generated by the periodic horizontal oscillations of a sphere in a linearly stratified fluid. J Fluid Mech 263(3):245–270

Martin S, Simmons WF, Wunsch CI (1969) Resonant internal wave interactions. Nature 224(5223):1014–1016

Maurer P, Ghaemsaidi SJ, Joubaud S, Peacock T, Odier P (2017) An axisymmetric inertia-gravity wave generator. Exp Fluids 58(10):1–14

McEwan AD (1971) Degeneration of resonantly-excited standing internal gravity waves. J Fluid Mech 50(3):431–448

McEwan AD (1973) Interactions between internal gravity waves and their traumatic effect on a continuous stratification. Bound Layer Meteorol 5(1–2):159–175

Mercier MJ, Martinand D, Mathur M, Gostiaux L, Peacock T, Dauxois T (2010) New wave generation. J Fluid Mech 657:308–334

Mowbray DE, Rarity BSH (1967) A theoretical and experimental investigation of the phase configuration of internal waves of small amplitude in a density stratified liquid. J Fluid Mech 28(1):1–16

Nikurashin M, Ferrari R (2013) Overturning circulation driven by breaking internal waves in the deep ocean. Geophys Res Lett 40(12):3133–3137

Phillips OM (1960) On the dynamics of unsteady gravity waves of finite amplitude. J Fluid Mech 9(2):193–217

Scorer RS (1949) Theory of waves in the lee of mountains. Q J R Meteorol Soc 75(323):41–56

Smith S, Crockett J (2014) Experiments on nonlinear harmonic wave generation from colliding internal wave beams. Exp Therm Fluid Sci 54:93–101

Staquet C, Sommeria J (2002) Internal gravity waves: from instabilities to turbulence. Annu Rev Fluid Mech 34:559–593

Sutherland BR (2010) Internal gravity waves. Cambridge University Press, Cambridge

Sutherland BR, Dalziel SB, Hughes GO, Linden PF (1999) Visualization and measurement of internal waves by 'synthetic schlieren'. Part 1. Vertically oscillating cylinder. J Fluid Mech 390:93–126

Tabaei A, Akylas TR, Lamb KG (2005) Nonlinear effects in reflecting and colliding internal wave beams. J Fluid Mech 526:217–243